Electronic Supplementary Material (ESI) for Chemical Science.

Synthesis of a d^2 kagome lattice antiferromagnet, $(CH_3NH_3)_2NaV_3F_{12}$

Ningxin Jiang,[a] Arun Ramanathan,[a] Ryan E. Baumbach,[b] Henry S. La Pierre*[a,c]

[a] School of Chemistry and Biochemistry, Georgia Institute of Technology, Atlanta, Georgia 30332-0400, United States.

[b] National High Magnetic Field Laboratory, Tallahassee, Florida, 32306, USA

[c] Nuclear and Radiological Engineering and Medical Physics Program, School of Mechanical Engineering, Georgia Institute of Technology, Atlanta, Georgia 30332-0400, United States.

Contents

1. Experimental details

General Methods. All reagents were obtained from commercial suppliers without further purification. Deionized water with a resistivity of 18.2 MΩ·cm was used for all syntheses. Hydrothermal reactions were carried out in 23 mL Teflon-lined pressure vessels (Parr 4749) purchased from Parr Instruments.

Caution! Hydrofluoric acid is toxic and corrosive and must be handled using the appropriate protective gear and training.[1-3] All the experiments including the hydrothermal reactions should be conducted in well-ventilated fume-hoods and calcium gluconate gel must be immediately available in case of accidental exposure.

Synthesis of $(CH_3NH_3)_2NaV_3F_{12}$, 1-V. Single-crystals of $(CH_3NH_3)_2NaV_3F_{12}$ were synthesized by the hydrothermal method. V_2O_5 powder (145.5 mg, 0.8 mmol), NaF (21.0 mg, 0.5 mmol), CH_3NH_2·HCl (135.0 mg, 2.0 mmol) were added to a 23 mL Teflon liner and dissolved with 0.5 mL of 48% HF at room temperature after shaking the liner continuously for 5 minutes. To the resultant light-yellow solution, 2 mL of deionized water and 2 mL of ethylene glycol (EG) were added which resulted into an orange solution. The Teflon vessel with solution was sealed in the stainless-steel Parr vessel. The vessel was put in a pre-heated, gravity convection oven at 453 K for 42 hours under autogenous pressure and then cooled to room temperature at a rate of 0.5 K / minute. Brown-green crystals of **1-V** with black impurities were observed in the liner after the reaction. The solid products are isolated by vacuum filtration. The black impurities can be separated from the brown-green crystals by dispersing the solid products into deionized water and decanting the supernatant of the resulting mixture several times until the product is free of the floating black impurities. The crystals were washed with ethanol and then air dried for 30 minutes to afford 88.4 mg of **1-V** (35% yield based on vanadium). Bulk purity of the as-synthesized **1-V** was confirmed by comparing the experimental PXRD pattern with the simulated PXRD pattern based on single crystal X-ray diffraction result measured at 300 K. (Figure S2).

Synthetic Notes: The initial attempts for the preparation of **1-V** based on the modified protocol from the synthesis of **1-Ti**[4] (hydrothermal synthesis with V metal or V_2O_3, CH_3NH_2·HCl, NaF, HPF_6 and water) resulted in only Na_3VF_6. The employment of EG is important since it not only serves as a moderate reducing agent for the slow generation of V^{3+} but may also be crucial for crystal growth by tuning the solubility of all the intermediates. The black impurities in the synthesis **1-V** could be the organic impurities from ethylene glycol since no additional peaks can be observed in powder X-ray diffraction (PXRD) patterns in the presence of these black impurities.

2. Crystallographic data and analysis

Single Crystal X-ray Diffraction (SCXRD). Single crystal of **1-V** was adhered to Mitogen loops with Paratone oil and then mounted on a goniometer under a cold stream at 100 K or 300 K. The crystal was then optically aligned on a Bruker D8 Quest X-ray diffractometer using a digital camera. Diffraction data were obtained with an X-ray source (Mo Kα, λ = 0.71073 Å) with high brilliance and high-performance focusing multilayered optics. APEX 3 was used for determination of unit cells, data collection, and integration of the data. Numerical absorption corrections were also applied with SADABS.[5] Two twelfth sphere of data was collected for both structures. The structures were solved using the ShelXT structure solution program using the Intrinsic Phasing solution method and by using Olex2 as the graphical interface.[6] The models were refined with version 2014/7 of ShelXL 2014 using Least Squares minimization.[7]

Powder X-ray Diffraction (PXRD). Powder X-ray diffraction patterns were obtained with a PANalytical X'Pert PRO Alpha-1 diffractometer using a 1.8 kW ceramic copper tube source. The simulated PXRD patterns from SCXRD results are performed using software CrystalDiffract 6.80.

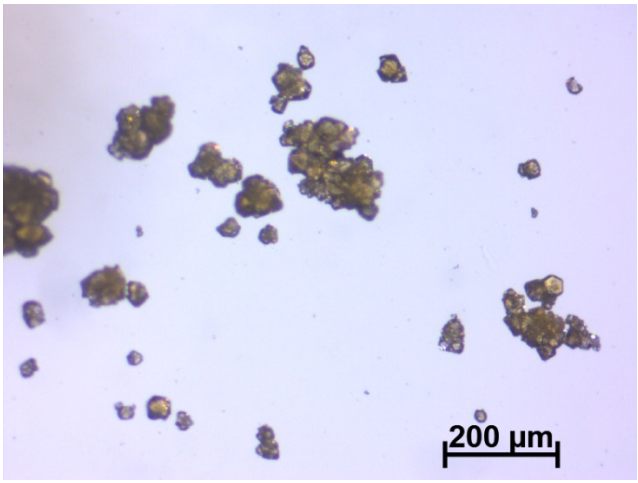

Figure S1. Crystals of **1-V**. The picture was acquired with a ZEISS Stereo microscope (Stemi 508) and a ZEISS Axiocam ERc 5s microscope camera.

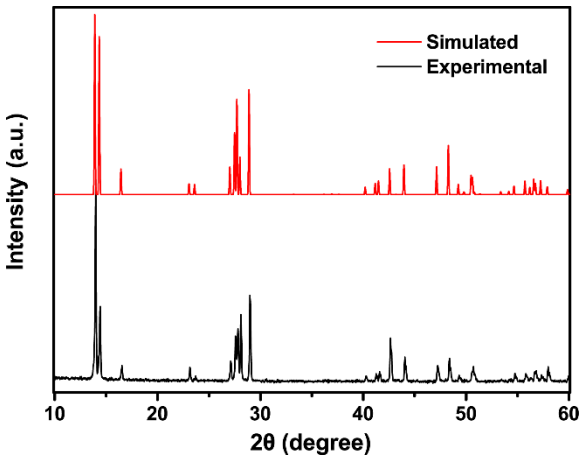

Figure S2. Experimental (black line) and simulated (red line) PXRD patterns based on the SCXRD results under 300 K for **1-V**. No difference can be observed between the simulated result and the experimental data which suggests that accuracy of the SCXRD result and the bulk purity of as-synthesized **1-V** samples.

Table S1. Crystal data and structure refinement for **1-V** at 300 K and 100 K.

Compound	**1-V**	**1-V-100 K**
Empirical formula	$(CH_3NH_3)_2NaV_3F_{12}$	$(CH_3NH_3)_2NaV_3F_{12}$
$D_{calc.}$/ g cm^{-3}	2.482	2.507
m / mm^{-1}	2.365	2.389
Formula Weight	467.92	467.92
Color	Brown green	Brown green
Shape	Prism	Prism
Size / mm^3	0.187 × 0.14 × 0.124	0.187 × 0.14 × 0.124
T / K	300	100
Crystal System	Trigonal	Trigonal
Space Group	$R\bar{3}$m	$R\bar{3}$m
a / Å	7.5349(13)	7.5156(5)
b / Å	7.5349(13)	7.5156(5)
c / Å	19.100(3)	19.0063(12)
α / °	90	90
β / °	90	90
γ / °	120	120
V / Å^3	939.1(4)	929.73(14)
Z	3	3
Z'	0.08333	0.08333
F(000)	678.0	678.0
Radiation	MoKα (λ = 0.71073 Å)	MoKα (λ = 0.71073 Å)
2θ range for data collection (°)	7.564 to 80.534	6.432 to 80.384
Index Ranges	-13 ≤ h ≤ 12, -13 ≤ k ≤ 13, -32 ≤ l ≤ 34	-13 ≤ h ≤ 13, -13 ≤ k ≤ 13, -15 ≤ l ≤ 34
Reflections Collected	3676	3120
Independent Reflections	761[R_{int} = 0.0335]	761[R_{int} = 0.0381]
Data/Restraints/Parameters	761/17/33	761/17/33
Goodness-of-Fit on F^2	1.112	1.173
Final R Indexes [I>=2σ (I)]	R_1 = 0.0300, wR_2 = 0.0727	R1 = 0.0321, wR2 = 0.0779
Final R Indexes [all data]	R_1 = 0.0340, wR_2 = 0.0762	R1 = 0.0351, wR2 = 0.0802
Largest Diff. Peak/Hole (e$^-$ / Å^3)	1.00 / -1.12	1.33 / -1.40
Completeness to 2θ	96.7%	99.6%

Table S2. Atomic coordinates of **1-V** at 300 K and 100 K (Hydrogen atoms are omitted for simplicity).

Atoms	Wyckoff positions	*x / a*	*y / b*	*z / c*	U_{eq}
300 K					
V1	9*e*	0.166667	0.333333	0.333333	0.01167(9)
Na1	3*b*	0	0	0.5	0.0129(2)
F1	18*h*	0.14287(10)	0.2857(2)	0.43063(6)	0.0273(2)
F2	36*i*	0.45670(9)	0.54330(9)	0.34598(6)	0.0231(2)
C0	6*c*	0.666667	0.333333	0.4356(6)	0.0496(17)
C1	36*i*	0.707(3)	0.353(4)	0.4493(8)	0.0496(17)
N1	18*h*	0.5774(5)	0.4226(5)	0.4795(3)	0.0382(11)
100 K					
V1	9*e*	0.833333	0.666667	0.666667	0.00587(9)
Na1	3*b*	1	1	0.5	0.0042(2)
F1	18*h*	0.85785(9)	0.71570(19)	0.56903(5)	0.01439(19)
F2	36*i*	0.54309(8)	0.45691(8)	0.65360(6)	0.01254(18)
C0	6*c*	0.666667	0.333333	0.4388(5)	0.0261(13)
C1	36*i*	0.7036(19)	0.356(3)	0.4490(7)	0.0261(13)
N1A	9*e*	0.5755(4)	0.4245(4)	0.4806(2)	0.0197(8)

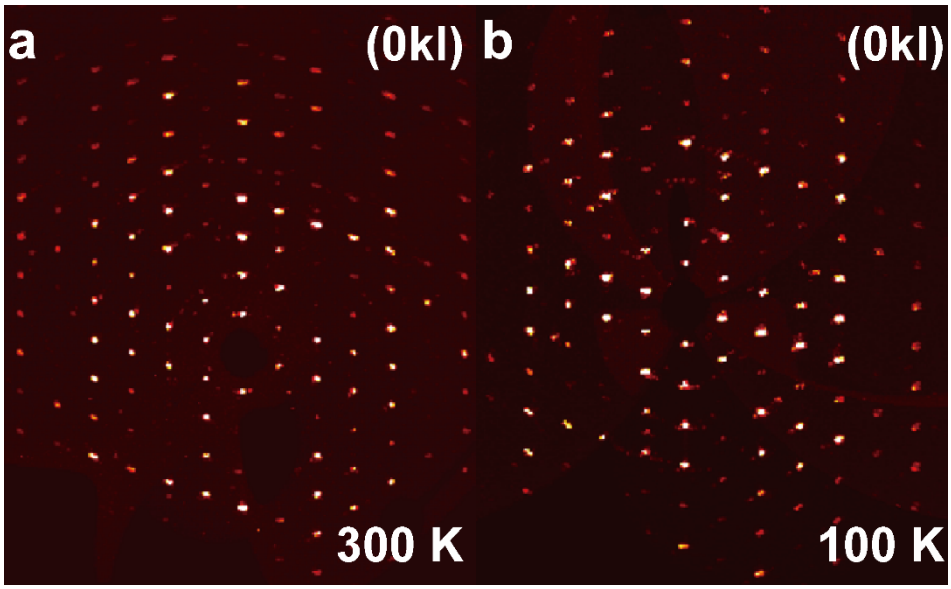

Figure S3. The precession image of (0kl) plane calculated from SCXRD data at (a) 300 K and (b) 100 K.

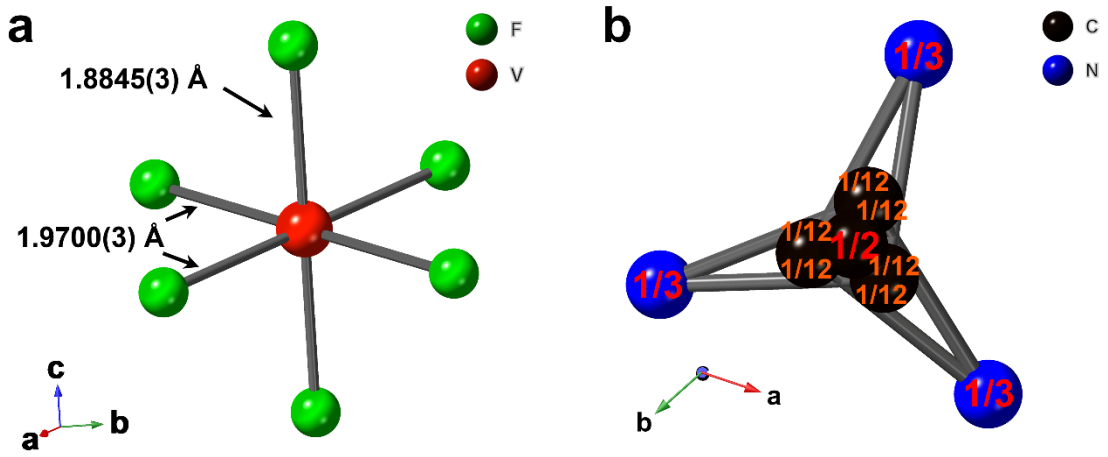

Figure S4. (a) The coordination environments of VF_6^{3-} in **1-V**. (b) Demonstration of the disorder model for MA^+ with the occupancy of carbon and nitrogen sites in the center of the atoms viewed parallel to the crystallography *c*-axis in **1-V**.

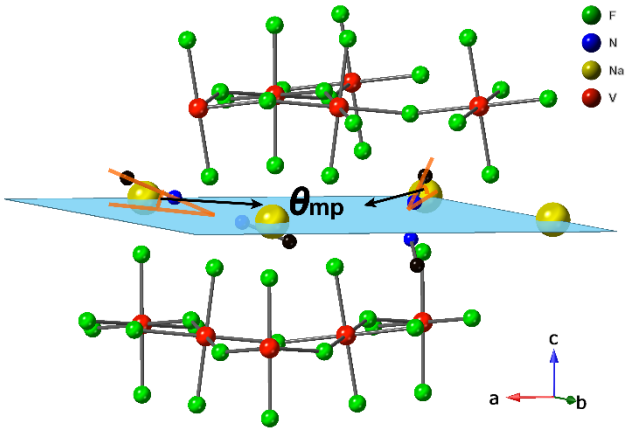

Figure S5. Demonstration of the θ_{mp} (the angle between C–N bond of MA^+ and (001) crystal plane in **1-V**) in **1-V**.

3. Fourier-transformation infrared spectroscopy

Fourier-Transformation Infrared Spectroscopy (FT-IR). Infra-red samples were acquired as powders on a Bruker ALPHA FTIR spectrometer from 360 to 4000 cm^{-1} in ambient condition. The sample was dried under vacuum conditions using Schlenk techniques for 15 minutes prior to the measurement.

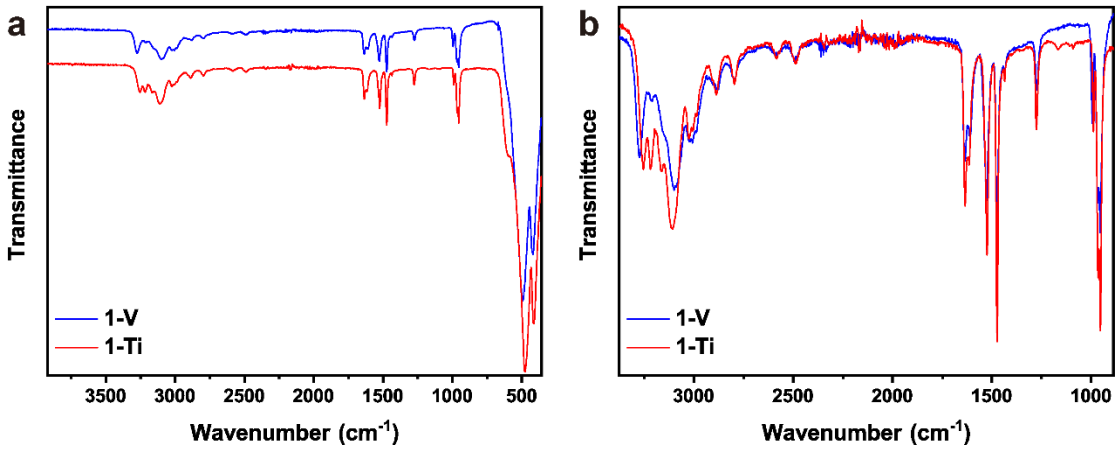

Figure S6. (a) FT-IR spectra for **1-V** and **1-Ti**. (b) The zoom-in FT-IR spectra for **1-V** and **1-Ti**. In both figures, the transmittance has been rescaled.

The bands observed in **1-V** and **1-Ti** are similar in position and intensity due to the similar composition and crystal structure of these two compounds.[4] The bands centered at 492 cm^{-1} in **1-V** which is assigned to the M-F vibrational modes shifts to 475 cm^{-1} in **1-Ti** which can be ascribed to the change of metal identity. The shift of band positions and the change of the transmittance can be observed between 3500 cm^{-1} and 2800 cm^{-1} in **1-Ti** and **1-V**. These bands are characteristic vibration bands for $CH_3NH_3^+$ cations and the change in these features might be due to the change of the tilting angles for $CH_3NH_3^+$ cations and their respective H–F bonding interactions.

4. X-ray photoelectron spectroscopy

X-ray photoelectron spectroscopy data were recorded using a Thermo K-Alpha spectrometer with an Al Kα source (*hv* = 1486.6 eV). The peak fit was conducted in the Thermo Scientific TM Avantage software. The adventitious C 1s at 284.8 eV was used as a reference for the binding energies as shown in Fig. S7(a). A Shirley background is applied in the peak fitting process.

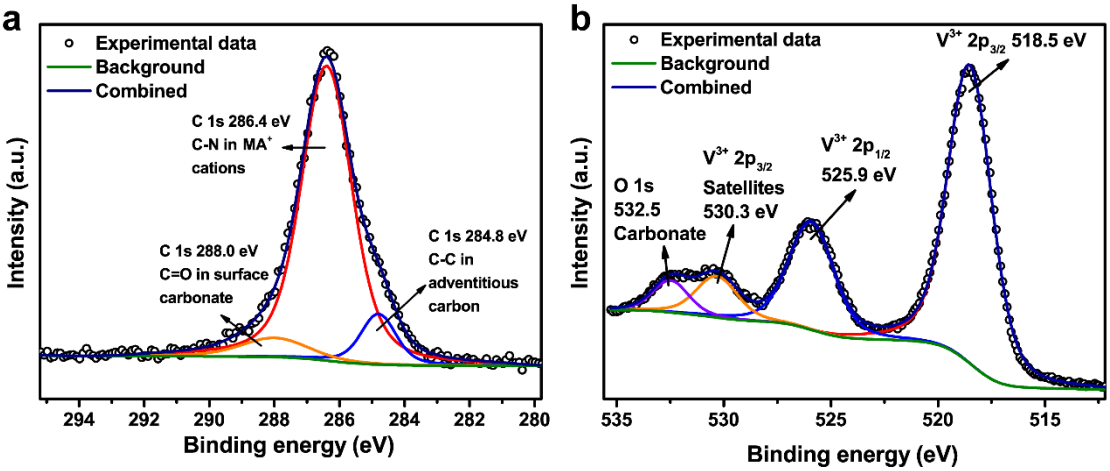

Figure S7. High resolution XPS (a) C 1s and (b) V 2p spectra of **1-V**.

The high-resolution XPS C1s and V 2p spectra of **1-V** are shown in Fig. S7.

The XPS C1s spectrum is resolved into three peaks. The peak centers at 248.8 eV can be assigned as the adventitious carbon species and is used as a reference for the binding energies. The peak centers at 286.4 eV is assigned as the carbon in C-N bonds in MA^+ cations. The peak centers at 288.0 eV is assigned as the surface carbonate as the sample was exposed to air before the measurement.

The presence of O 1s intensity in the V 2p spectra can be observed in vanadium fluoride sample that was exposed in air and affects the accuracy of peak fitting.[8] A Shirley background is used here for peak fitting and the spectrum can be resolved into four peaks.[9] The peak centers at 532.5 eV is assigned as the surface carbonate which is assigned as the surface carbonate. The peaks center at 518.5 eV and 530.3 eV are assigned as the V^{3+} $2p_{3/2}$ and the V^{3+} $2p_{3/2}$ satellites which match well with the reported value.[10] The V 2p peak has significantly split spin-orbit component and ΔE is ~7.5 eV between V^{3+} $2p_{3/2}$ and V^{3+} $2p_{1/2}$. Therefore, the peak centers at 525.9 eV can be assigned as V^{3+} $2p_{1/2}$. Inclusion of extra peaks that represents V^{2+} or V^{4+} species results in poor fitting result suggest the absence of these species.

5. UV-vis-NIR diffuse reflectance spectroscopy

UV-vis-NIR diffuse reflectance spectra (UV-vis-NIR DRS) of the **1-V**, **1-Ti**, and $CH_3NH_2 \cdot HCl$ were recorded on a UV-vis-NIR spectrophotometer (UH4150, Hitachi) with an integrating sphere attachment within the range of 200-2600 nm and $BaSO_4$ was used as the reflectance standard.

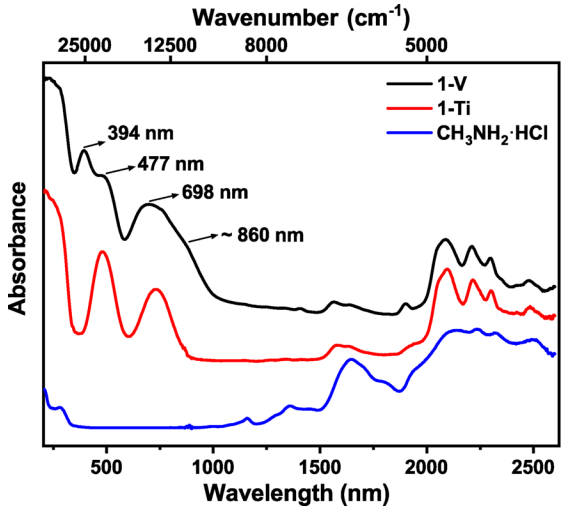

Figure S8. UV-vis-NIR diffuse reflectance spectra of **1-V**, **1-Ti** and $CH_3NH_2 \cdot HCl$. Inset: Proposed local 3d orbital splitting diagram in **1-V** based on the UV-vis-NIR DRS data.

The UV-vis-NIR DRS of **1-V** is employed to study the *d*-orbital splitting of the 3*d* orbitals and the **1-Ti** and $CH_3NH_2 \cdot HCl$ were used reference compounds as shown in Fig S6. Thirteen peaks can be observed for the spectrum of **1-V**. All the absorptions above 1500 nm are attributed to the feature of MA^+ cations which **1-V** can be clearly observed in both **1-Ti** and $CH_3NH_2 \cdot HCl$.[4, 11] The absorptions below 340 nm is ascribed to ligand to metal charge transfer. The absorptions at 394 nm, 477 nm, 698 nm and 860 nm matches well with the transitions observed in KVF_4 and $CsVF_4$ which indicates that five 3d orbitals are split to four different energy levels due to the compressed octahedra fluoride ligand environment which supports the trivalent oxidation state assignment and the S = 1 spin state for vanadium cations in **1-V**. The orbital parentage of the ground is not firmly established in the literature. The simulations and theoretical modeling of Babel and co-workers[12] on the spectrum of in KVF_4 in particular are consistent with a ^3E_g ground state.

6. Thermal analysis.

The differential scanning calorimetry (DSC) measurements were carried out using Mettler Toledo instruments TGA/DSC 3+ with the scanning rate of 1 K / min on cooling / heating in the temperature range of 183 – 363 K. The scans were all performed in flowing nitrogen (flow rate: 80 mL / min).

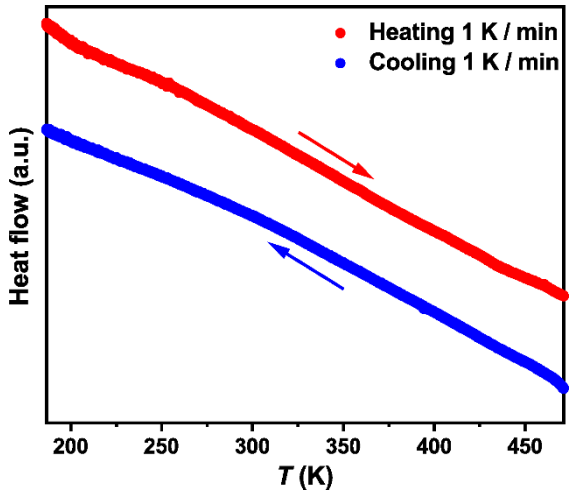

Figure S9. DSC curves for **1-V**, blue dots represent the cooling curve, and the red dots represent the heating curve (temperature range from 183 K to 473 K, scanning rate: 1 K / min).

7. Magnetic properties

Physical properties measurement. The dc magnetic susceptibility, ac magnetic susceptibility, magnetization measurements and mangetic ageing experiments were performed on the **1-V** samples composed of small single crystals using a Quantum Design physical property measurement system (PPMS) and Mangetic properties measurement systems (MPMS) in a range of magnetic fields $0 \leq \mu_0 H \leq 14$ T and temperatures $1.8 \leq T \leq 300$ K. For the isothermal magnetization measurement at 1.8 K, the scan rate is 32 Oe/s. The heat capacity measurements were carried out on a Quantum Design PPMS with a pellet of **1-V** under 0 T and 9 T. For the magnetic ageing experiment, the sample was cooled from 50 K to the measurement temperature, T_m, under zero magnetic field, after waiting time t_w, a magnetic field of 0.0025 T was applied and the time evolution of magnetic moment of the system was recorded.

The Curie-Weiss temperature θ_{cw} was derived from the fitting of dc magnetic susceptibility data between 150 K and 300 K with the modified Curie-Weiss law, $\chi = C / (T - \theta_{cw}) + \chi_0$; C is the Curie constant, θ_{cw} is the Curie-Weiss temperature and χ_0 is the temperature independent term. Fitting the temperature dependence of dc magnetic susceptibility data from 150 K to 300 K with modifield Curie-Weiss law yields a θ_{cw} of -39(3) K. Various initial values of χ_0 were used for the fitting and all lead to same θ_{cw}. The dc susceptibility data was also fitted to the normal Curie-Weiss law, $\chi = C / (T - \theta_{cw})$, from 200 K to 300 K with θ_{cw} = -116(2) K. The magnetic effective moment, μ_{eff}, was derived from the following equation, $\mu_{eff} = (8C)^{1/2}$.

The empirical parameter X, which is used to express the frozen temperature observed in χ' vs. frequency dependence, is calculated based on the equation, $X = \Delta T_f / [T_f \Delta(\log \omega)]$, where ω is the frequency used in the measurement and T_f is the frozen temperature. The T_f was determined by calculating the first derivative of χ' vs. temperature dependence and the minimum of the absolute value for the first derivative is the frozen temperature. The T_f is 3.340 when ω = 4992 Hz, 3.265 when ω = 2002 Hz, 3.205 when ω = 1001 Hz, 3.103 when ω = 500 Hz and 3.064 when ω = 200 Hz. The X = 0.059 when $X = (T_{f,4992Hz} - T_{f,200Hz}) / \{T_{f,4992Hz} * [\log(4992) - \log(200)]\}$.[13]

The time-dependence of magnetic moment change curves under 1.8 K were fitted to the stretched exponential function as shown in equation (1).[14]

$$M(t) = M_0 + M_r e^{-(\frac{t}{\tau})^{\alpha}} \qquad (1)$$

The M_0 is the intrinsic magnetic compenent, M_r and τ are the glassy component and characteristic relaxation time, α is the stretching parameter.

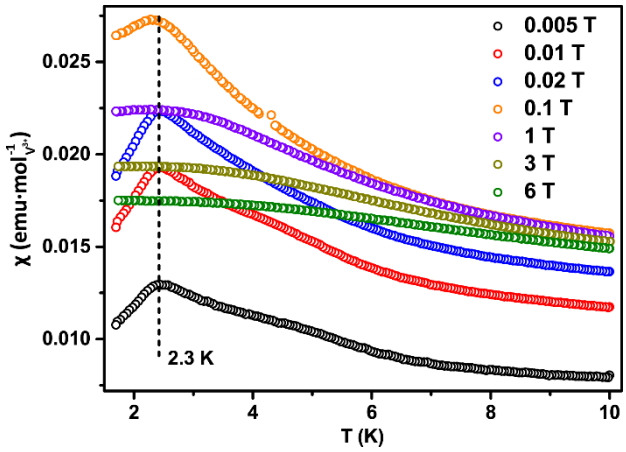

Figure S10. Temperature dependence of magnetic susceptibility in **1-V** as measured under FC condition under different applied magnetic field from 0.005 T to 6 T.

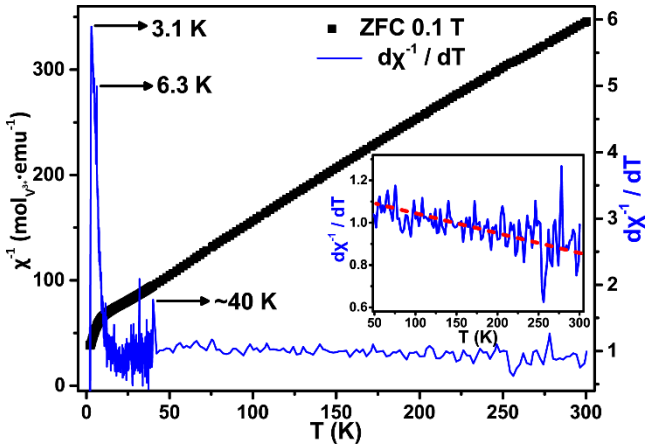

Figure S11. Temperature dependence of inverse magnetic susceptibility under ZFC condition and 0.1 T (left axis, black dot) and the differential susceptibility dχ^{-1} / dT curves (right axis, blue line) from 1.8 K to 300 K in **1-V**. Inset: The differential susceptibility dχ^{-1} / dT curves from 1.8 K to 25 K in **1-V** under ZFC condition. The red line is shown to guide the eye.

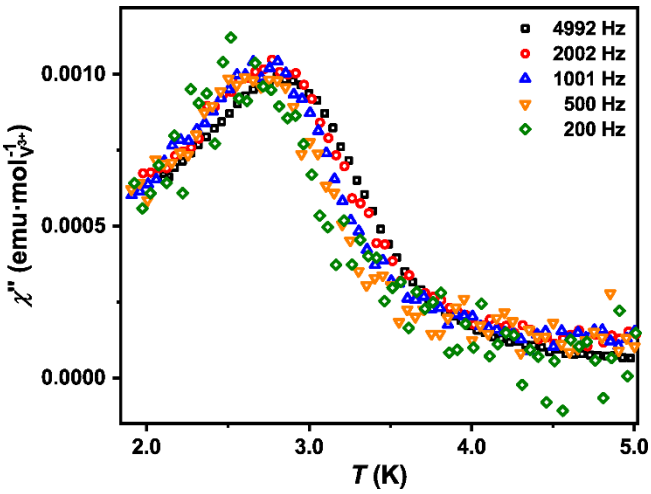

Figure S12. The temperature dependence of the imaginary part of ac susceptibility from 1.8 K to 5 K under 0 T with different frequencies in **1-V**.

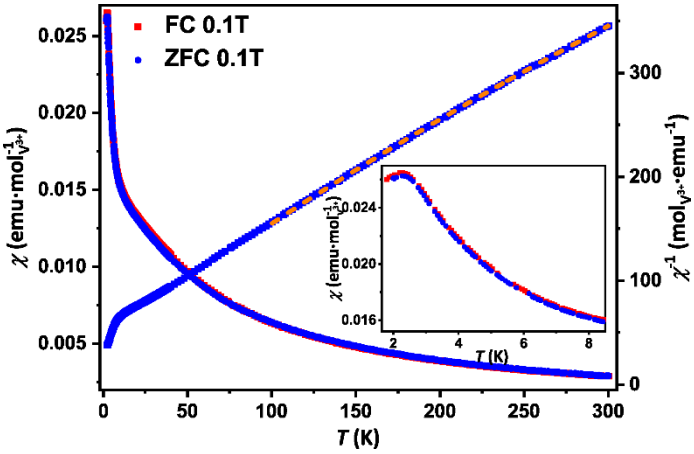

Figure S13. Temperature dependence of magnetic susceptibility in **1-V** under 0.1 T ZFC and FC conditions (left axis). Temperature dependence of inverse magnetic susceptibility under ZFC condition and 0.1 T (right axis). The dashed orange line is the modifield Curie-Weiss fit from 150 K to 300 K. Inset: Temperature dependence of magnetic susceptibility from 1.8 K to 8 K in 1-V under 0.1 T FC and ZFC condition.

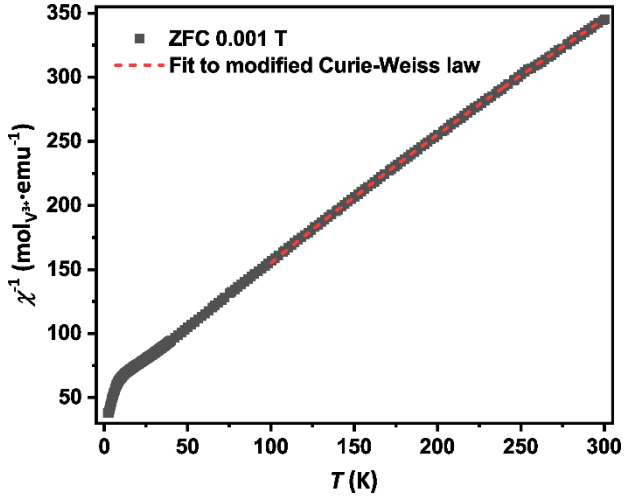

Figure S14. Temperature dependence of inverse magnetic susceptibility under ZFC condition and 0.001 T in **1-V**. The dashed red line is the modified Curie-Weiss fit from 150 K to 300 K.

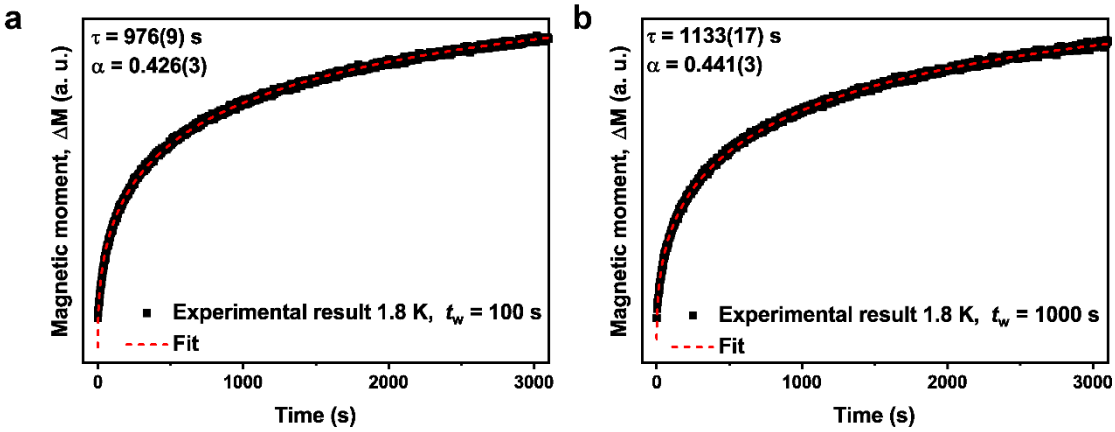

Figure S15. Time dependence of magnetic magnetic moment change in **1-V** with waiting time of (a) 100 s and (b) 1000 s. The black dots are experimental data and the dashed red lines are fitting results to the stretched expentional function as shown in equation (1).

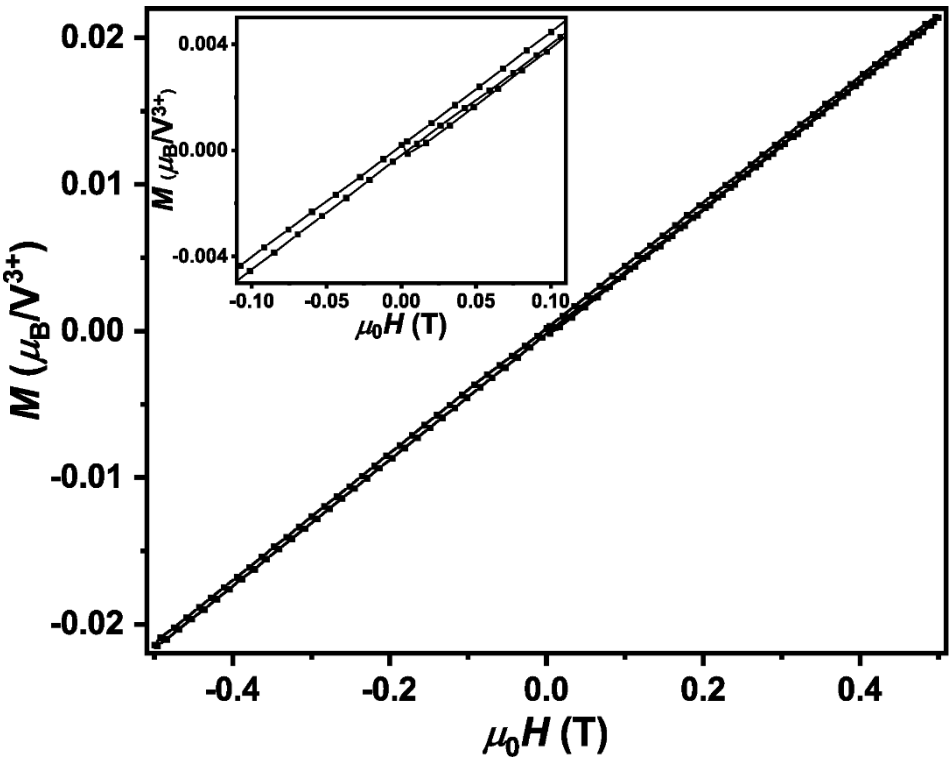

Figure S16. Magnetic field dependence of magnetization in **1-V** at 1.8 K from 0 T to 0.5 T, 0.5 T to -0.5 T and -0.5 T t 0.5 T.

Table S3. Physical properties comparison of **1-V** and **1-Ti**[4]

	1-V	**1-Ti**
Spin	1	1/2
Curie-Weiss temperature (K)	-39(3)	-139.5(7)
Long-range magnetic ordering	No	No
Frustration parameter	16.2	>1390
ac Magnetic susceptibility	Frequency dependence and peak observed around 3.5 K	Frequency dependence and no peak observed down to 1.8 K
Magnetization at 1.8 K under 14 T (μ_B/M^{3+})	0.383	0.101
Defect-like spin percentage (assume S = 1 in **1-V** and S = 1/2 in **1-Ti** for these spins)	2.84(3)	4.7(4)

8. References

1. Bertolini, J. C., Hydrofluoric acid: a review of toxicity. *J. Emerg. Med.* **1992,** *10* (2), 163-168.
2. Segal, E. B., First aid for a unique acid, HF: A sequel. *Chem. Health Saf.* **2000,** *7* (1), 18-23.
3. Peters, D.; Miethchen, R., Symptoms and treatment of hydrogen fluoride injuries. *J. Fluorine Chem.* **1996,** *79* (2), 161-165.
4. Jiang, N.; Ramanathan, A.; Bacsa, J.; La Pierre, H. S., Synthesis of a d^1-titanium fluoride kagome lattice antiferromagnet. *Nat. Chem.* **2020**, 12, 691-696.
5. Sheldrick, G. M., SADABS, program for empirical absorption correction of area detector data. **1996**.
6. Sheldrick, G. M., SHELXT: Integrating space group determination and structure solution. *Acta Crystallogr., Sect. A: Found. Adv* **2014,** *70*, C1437.
7. Sheldrick, G. M., Crystal structure refinement with SHELXL. *Acta Crystallogr. C* **2015,** *71* (1), 3-8.
8. Beamson, G.; Moslemzadeh, N.; Weightman, P.; Watts, J., Al Kα and Cu Kα1 excited XPS of vanadium oxide and VF_3 powders: Measurement of the V1s–KLL Auger parameters. *J. Electron. Spectrosc. Relat. Phenom.* **2008,** *162* (1), 19-24.
9. Seah, M., Quantification of AES and XPS. *Practical surface analysis* **1990,** *1*, 201.
10. Qiu, S.; Yarmoff, J., Self-limiting growth of transition-metal fluoride films from the reaction with XeF_2. *Phys. Rev. B: Condens. Matter* **2001,** *63* (11), 115409.
11. Kesari, Y.; Athawale, A., Ultrasound assisted bulk synthesis of $CH_3NH_3PbI_3$ perovskite at room temperature. *Mater. Lett.* **2015,** *159*, 87-89.
12. Reinen, D.; Atanasov, M.; Köhler, P.; Babel, D., Jahn–Teller coupling and the influence of strain in T_g and E_g ground and excited states–A ligand field and DFT study on halide $M^{III}X_6$ model complexes [M= Ti^{III}–Cu^{III}; X= F^-, Cl^-]. *Coord. Chem. Rev.* **2010,** *254* (23-24), 2703-2754.
13. Mydosh, J. A., *Spin glasses: an experimental introduction*. CRC Press: 2014.
14. Khan, N.; Mandal, P.; Prabhakaran, D., Memory effects and magnetic relaxation in single-crystalline $La_{0.9}Sr_{0.1}CoO_3$. *Phys. Rev. B: Condens. Matter* **2014,** *90* (2), 024421.